Visible light sensitive SnO2/ZnCo2O4 material for the photocatalytic removal of organic pollutants in water

Benhebal, Hadj; Wolfs, Cédric; Kadi, Samir; Tilkin, Rémi G.; Allouche, Boualem; Belabid, Radhwane; Collard, Valérie; Felten, Alexandre; Louette, Pierre; Lambert, Stéphanie D.; Mahy, Julien G.

Published in:
Inorganics

DOI:
10.3390/INORGANICS7060077

Publication date:
2019

Document Version
Publisher's PDF, also known as Version of record

inorganics

MDPI

Article

Visible Light Sensitive $SnO_2/ZnCo_2O_4$ Material for the Photocatalytic Removal of Organic Pollutants in Water

Hadj Benhebal [1], Cédric Wolfs [2], Samir Kadi [3], Rémi G. Tilkin [2,4], Boualem Allouche [1], Radhwane Belabid [1], Valérie Collard [5], Alexandre Felten [6], Pierre Louette [6], Stéphanie D. Lambert [2] and Julien G. Mahy [2,*]

1 Département de Chimie, Université Ibn-Khaldoun, Tiaret 14000, Algérie; benhebalh@yahoo.fr (H.B.); aloucheboualem@gmail.com (B.A.); radhwaneradhwane1993@gmail.com (R.B.)
2 Department of Chemical Engineering–Nanomaterials, Catalysis and Electrochemistry, B6a, University of Liege, 4000 Liege, Belgium; cedric.wolfs@uliege.be (C.W.); rtilkin@uliege.be (R.G.T.); stephanie.lambert@uliege.be (S.D.L.)
3 Laboratoire de Physiologie Végétale Appliquée au Culture Hors Sol, Département des Sciences de la Nature et de la Vie, Université Ibn-Khaldoun, Tiaret 14000, Algérie; ksam792002@yahoo.fr
4 Interfaculty Research Center of Biomaterials (CEIB), University of Liège, 4000 Liège, Belgium
5 Center for Education and Research on Macromolecules, University of Liège, Cesam-RU, 4000 Liège, Belgium; vcollard@uliege.be
6 SIAM Platform, University of Namur, Rue de Bruxelles 61, 5000 Namur, Belgium; alexandre.felten@unamur.be (A.F.); pierre.louette@unamur.be (P.L.)
* Correspondence: julien.mahy@uliege.be; Tel.: +32-4-366-95-34

Received: 27 May 2019; Accepted: 19 June 2019; Published: 21 June 2019

Abstract: In this study, pure $ZnCo_2O_4$ and $SnO_2/ZnCo_2O_4$ mix photocatalysts have been synthesized by the sol-gel process with three different SnO_2 loading percentages (10, 20, and 30 wt %). Their photocatalytic activities were assessed on the degradation of organic pollutants in water under visible illumination. The structural, morphological, and optical properties were analyzed by X-ray diffraction (XRD), scanning electron microscopy, energy-dispersive X-ray (EDX), Fourier transform infrared (FTIR), nitrogen adsorption-desorption isotherms, X-ray photoelectron spectroscopy (XPS), and UV–Visible diffuse reflectance measurements. The results have shown that the materials are composed of a crystalline $ZnCo_2O_4$ matrix with a decrease in crystallite size with the amount of SnO_2. Weakly crystalline SnO_2 is also observed for loaded samples. The specific surface area is modified with the loading ratio. The evaluation of the photoactivity of the samples under visible light for the degradation of *p*-nitrophenol has highlighted that all materials are highly photoactive under visible light thanks to heterojunction between the two oxides. An application test has been conducted on a dye, congo red, showing the same tendencies. An optimal amount of SnO_2 loading is observed for the sample containing 20 wt % of SnO_2. A comparison with commercial Evonik P25 showed that the materials developed in this work have five to six times better efficiency under visible light, leading to a promising photocatalyst material.

Keywords: $ZnCo_2O_4$; SnO_2; sol-gel; photocatalysis; visible activity

1. Introduction

During the past decade, water pollution has been considered as an environmental problem that requires effective solutions [1]. The removal of toxic pollutants from wastewater is necessary for the protection of health and environment. Organic pollutants and, in particular, dyes are frequently

found in the wastewaters of several industries such as electroplating, textile production, cosmetics, and pharmaceuticals. In wastewater treatment, a large number of methods have been reported for effective removal of organic pollutants, including physical, chemical, and biological approaches such as volatilization, electrochemical treatment, hydrolysis, photolysis, oxidation, biodegradation, or adsorption.

Advanced oxidation processes (AOP) are efficient processes that eliminate non degradable organic pollutants by means of biological processes [2]. One of these solutions, heterogeneous photocatalysis, is nowadays recognized as a strategic area of growing importance regarding the development of sustainable technologies for energy water treatments [3]. Considerable efforts have been made to synthesize, characterize, and describe the physical and chemical properties of metal oxide nanomaterials because of their significant applications in numerous technological fields [4]. Many semiconductors, such as TiO_2, ZnO, SnO_2, WO_3, or CeO_2, have shown promising photocatalytic activity for organic pollutant degradation [5–7]. The most widely used photocatalyst is TiO_2 [8,9], which is a non-toxic and cheap semiconductor sensitive to UV radiation [10]. Due to its large band gap (3.2 eV → 388 nm, for anatase phase), when solar light is used, only 5–8% of the solar spectrum [10] can be used. For economic and ecological reasons, much effort is being devoted to developing the efficient use of solar light, targeting materials photoactive under visible illumination [8,11].

For this purpose, mixed metal oxides, resulting from the combination of metal oxides, with spinel structure and general formula AB_2O_4 like $MgAl_2O_4$, $CuGa_2O_4$, $CuFe_2O_4$, $ZnFe_2O_4$, $ZnMn_2O_4$, $MnCo_2O_4$, $NiCo_2O_4$, $CoMn_2O_4$, or $ZnCo_2O_4$, have been widely studied in recent years [12]. With its large absorption range (200–800 nm), the $ZnCo_2O_4$ material is a suitable candidate for photocatalysis application under solar radiation [13]. $ZnCo_2O_4$ nanoparticles are among the most promising materials for several technological and environmental applications [14]. Cubic spinel $ZnCo_2O_4$ is isomorphic to the Co_3O_4 crystal structure where Co^{2+} tetrahedral sites (Td) in Co_3O_4 is replaced by Zn^{2+} while the content of Co^{3+} in octahedral sites (Oh) remains unchanged [14,15]. To increase photoefficiency, combinations with other semiconductors have been also studied as $ZnO/ZnCo_2O_4$ [16], $TiO_2/ZnCo_2O_4$ [17], or $ZrO_2/ZnCo_2O_4$ [18] mixing.

The sol-gel method is a very attractive chemical route due to its simplicity and flexibility in the use of different source materials that allow synthesizing amorphous and polycrystalline materials at low cost. As the name implies, the sol-gel process is the conversion of a sol to a gel. The sol-gel process is therefore a series of hydrolysis and condensation reactions of the inorganic alkoxide monomers that forms colloidal particles (sol) and converts them into a continuous network (gel) [19,20]. Indeed, this synthesis method has proven to be effective for the synthesis of a large range of oxide materials [21–24] in different shapes as powder, film, or monolith.

The aim of this present work is the development of efficient pure and $SnO_2/ZnCo_2O_4$ mix photocatalysts synthesized by a sol-gel process for the removal of organic pollutant in water. The synthesized materials need to be photoactive under visible irradiation ($\lambda > 400$ nm). $ZnCo_2O_4$ and $SnO_2/ZnCo_2O_4$ nanocrystalline materials were synthesized by the sol-gel process. Three different contents of SnO_2 were studied: 10, 20, and 30 wt %. The resulting materials were characterized by X-ray diffraction (XRD), nitrogen adsorption-desorption measurements, Fourier-transformed infrared spectroscopy (FTIR), scanning electron microscopy coupled with an energy dispersive X-ray (SEM/EDX), X-ray photoelectron spectroscopy (XPS) and diffuse reflectance measurements. The photoefficiency was assessed based on the photodegradation of *p*-nitrophenol (PNP) under visible light. An application test was carried out on an industrial dye, congo red (CR). Congo red dye and *p*-nitrophenol are model pollutants found in literature [25–28]. However, congo red is a dye and can be affected by the process of sensitization, making it difficult to control whether the observed degradation is due to photocatalysis or not [29]. The recycling property of the catalysts was also assessed on the PNP degradation after five cycles of reaction (120 h of illumination).

2. Results and Discussion

2.1. Morphology and Composition

Theoretical and actual loading of SnO_2 are similar for each sample (Table 1). This means that SnO_2 is fully integrated into the material and no loss occurs during the synthesis.

Table 1. Sample composition and textural properties.

Samples	SnO_2 Theoretical Content (wt %)	SnO_2 Actual Content (wt %)	S_{BET} ($m^2 \cdot g^{-1}$) ±5	V_{DR} ($cm^3 \cdot g^{-1}$) ±0.01	d_{XRD} (nm) ±1
Pure $ZnCo_2O_4$	-	-	17	0.01	30
$ZnCo_2O_4/SnO_2$-10%	10	11	27	0.02	24
$ZnCo_2O_4/SnO_2$-20%	20	20	48	0.03	16
$ZnCo_2O_4/SnO_2$-30%	30	32	45	0.03	16

S_{BET}: Specific surface area determined by the BET method; V_{DR}: Specific micropore volume determined by Dubinin–Raduskevitch theory; d_{XRD}: Mean diameter of TiO_2 crystallites measured by the Scherrer method.

The XRD patterns of all samples are represented on Figure 1.

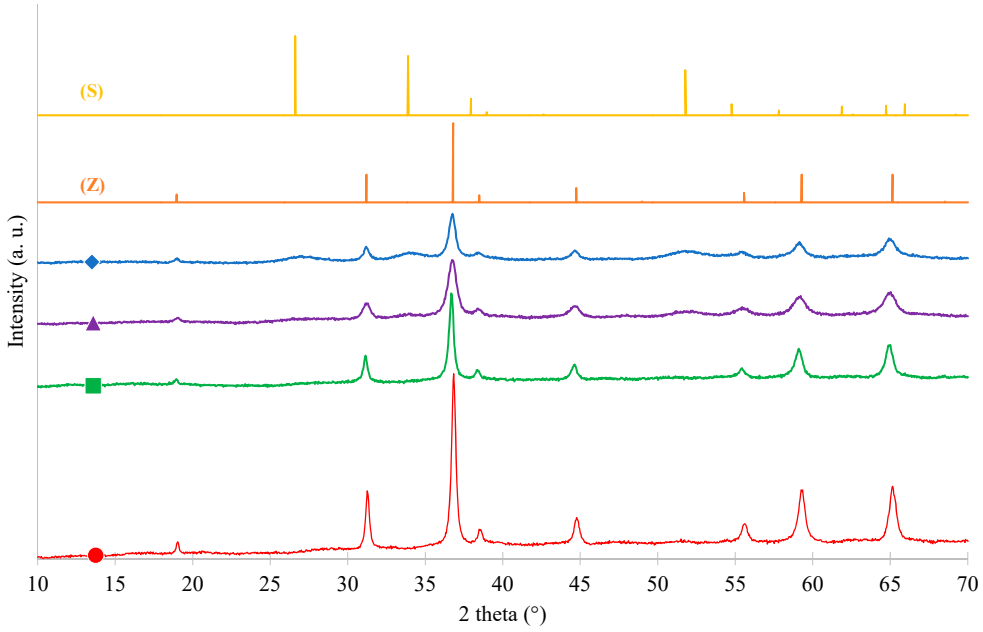

Figure 1. X-ray diffraction (XRD) patterns of samples: (●) Pure $ZnCo_2O_4$, (■) $ZnCo_2O_4/SnO_2$-10%, (▲) $ZnCo_2O_4/SnO_2$-20% and (♦) $ZnCo_2O_4/SnO_2$-30%. (Z) Reference pattern of cubic spinel $ZnCo_2O_4$ and (S) reference pattern of tetragonal rutile SnO_2.

All of the diffraction peaks illustrated by the four spectra at values of 18.951°, 31.190°, 36.750°, 44.691°, 55.503°, 59.192°, and 65.050° can be assigned to (111), (220), (311), (400), (422), (511), and (440) planes of cubic spinel $ZnCo_2O_4$ (JCPDS card No. 23-1390; space group Fd3m and a = 8.10440 Å) [30]. The sharp and strong XRD peaks are indicative of a high crystallinity and high purity of the nanocrystalline samples [31]. The $ZnCo_2O_4$ crystallite size (d_{XRD}) can be calculated with Scherrer equation (Equation (4)) with the peak at 31.190°. The different values are listed in Table 1. The crystallite size decreases (from 30 to 16 nm) when the SnO_2 amount increases (from 0 to 30 wt %), as observed on Figure 1, corresponding to the decreasing peak heights with the loading percentage. The introduction of SnO_2 in $ZnCo_2O_4$ matrix probably disturbs the crystallization and slows the growth rates of the crystals as observed in previous studies when dopants were added [32].

An additional diffraction peak corresponding to tetragonal rutile structure of SnO_2 (JCPDS Card No: 41-1445) appears, for the loaded samples, at 2θ = 26.60° and 33.92° corresponding to the crystal planes (110) and (101) [33]. This revealed that phase segregation has occurred in the samples [34]. As expected, the intensity of SnO_2 peaks increases when the amount of SnO_2 increases. Nevertheless, the SnO_2 crystals are smaller that $ZnCo_2O_4$ with a size around 7 nm (calculated from the peak at 26.60°) for $ZnCo_2O_4/SnO_2$-30% sample.

The sample textural properties are given in Table 1 and the adsorption-desorption isotherms are represented in Figure 2. The pure $ZnCo_2O_4$ sample isotherm has a shape corresponding to a type II isotherm according to the BDDT classification [35]. Indeed, at high pressure, the adsorbed volume increases quickly (macroporous solid). This sample present also a hysteresis, which corresponds to the presence of mesopores. When the samples are loaded with SnO_2, the isotherms evolve towards a mixture between types I and IV isotherms according to the BDDT classification [35]. Indeed, at low relative pressure, a sharp increase, characteristic of type I isotherm, can be observed (microporous solid). The increase at high pressure is reduced and replaced by a plateau corresponding to type IV isotherm (mesoporous solid). The hysteresis is also modified and displaced towards lower relative pressure (smaller mesopores). This shows that the pore size range evolves towards smaller pores and higher specific surface area when loaded with SnO_2. Indeed, the S_{BET} and V_{DR} values for pure $ZnCo_2O_4$ sample are 17 $m^2 \cdot g^{-1}$ and 0.01 $cm^3 \cdot g^{-1}$, respectively, while they are 48 $m^2 \cdot g^{-1}$ and 0.03 $cm^3 \cdot g^{-1}$ for $ZnCo_2O_4/SnO_2$-20%, respectively (Table 1). The $ZnCo_2O_4/SnO_2$-20% sample has the highest specific surface area, which indicates that 20 wt % of SnO_2 could be an optimal value. This result is confirmed by the photocatalytic experiment in Section 3.3.

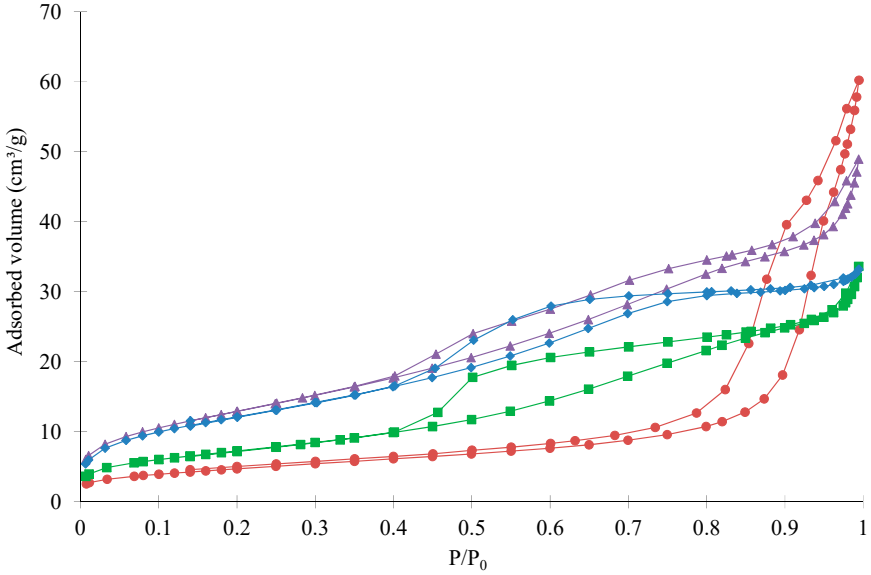

Figure 2. Nitrogen adsorption-desorption isotherms of samples: (●) pure $ZnCo_2O_4$, (■) $ZnCo_2O_4/SnO_2$-10%, (▲) $ZnCo_2O_4/SnO_2$-20% and (♦) $ZnCo_2O_4/SnO_2$-30%.

The morphology of the powders synthesized and calcined at 450 °C was studied by scanning electron microscopy. Figure 3 illustrates the SEM micrographs of pure $ZnCo_2O_4$ and $ZnCo_2O_4/SnO_2$-20% powders. The images clearly show that the particles have a generally spherical shape with irregular size distribution due to agglomerate formation. The sample particles are in the nanometric range, which supports the results obtained by XRD (d_{XRD}). The particle size is bigger for the pure $ZnCo_2O_4$ sample than the $ZnCo_2O_4/SnO_2$-20% one. It is in agreement with the crystallite size measured with XRD (Table 1).

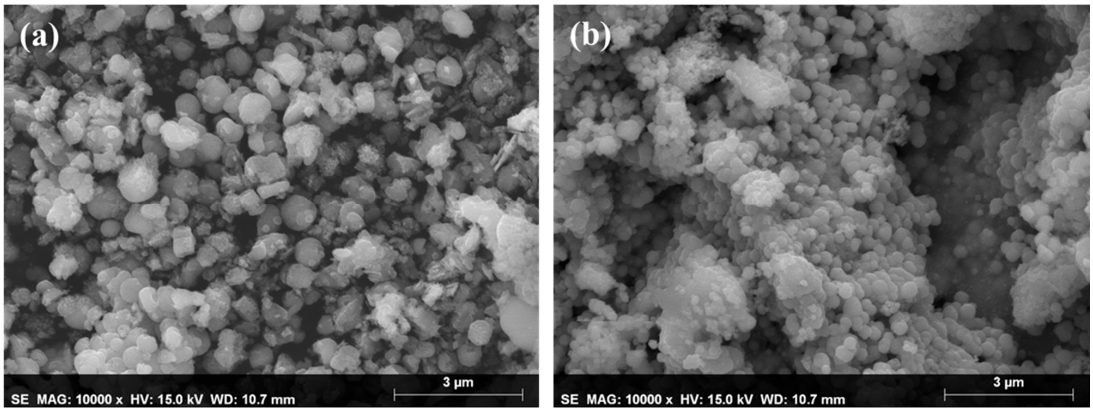

Figure 3. Scanning electron microscopy (SEM) images of as-synthesized pure $ZnCo_2O_4$ (**a**) and $ZnCo_2O_4/SnO_2$-20% (**b**) samples. The center of each picture corresponds to the place where the energy dispersive X-ray (EDX) analysis was carried out (see Figure 4).

In order to confirm the formation of the materials on the one hand and the effective presence of SnO_2 in the $SnO_2/ZnCo_2O_4$ nanomaterial on the other hand, an elemental analysis by EDX was also performed and represented in Figure 4. As shown in the spectra, the main elements (cobalt, zinc, and oxygen) are present in addition to tin in the $ZnCo_2O_4/SnO_2$-20% sample (Figure 4 right). The analysis also shows the presence of a small amount of carbon (C) and chlorine (Cl) bound mainly due to the precursors used in the synthesis.

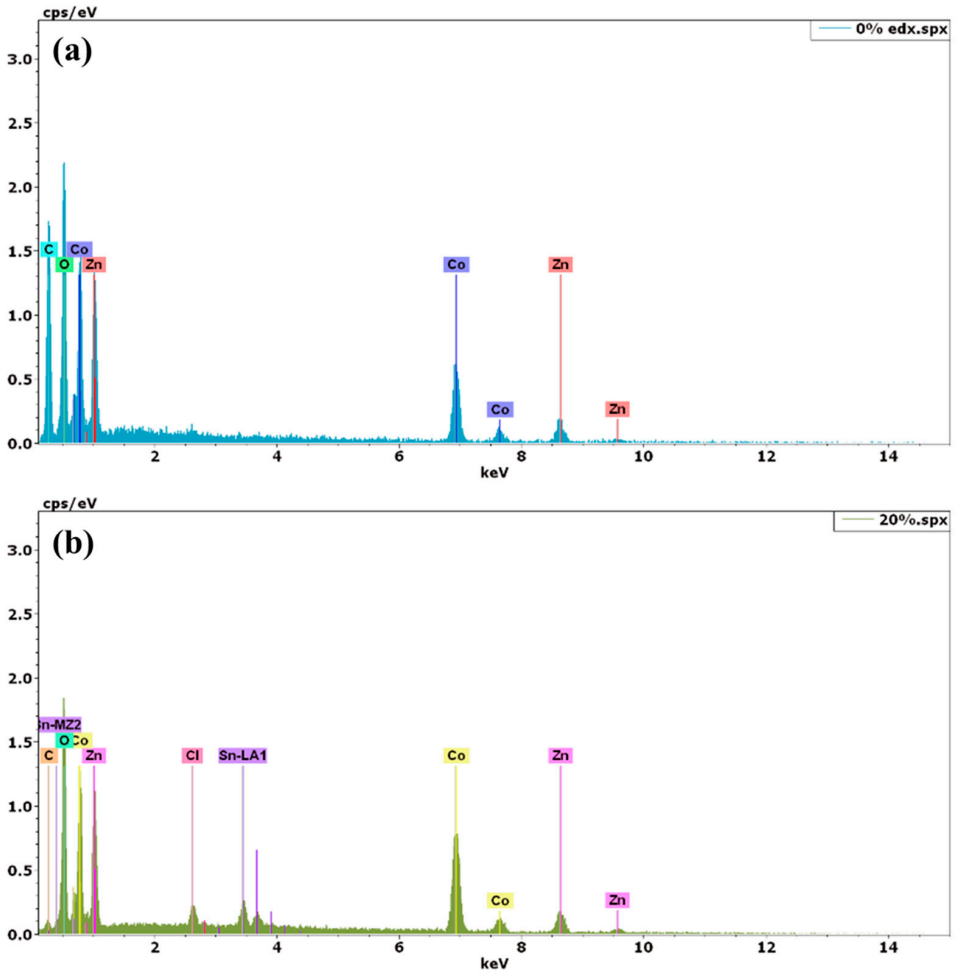

Figure 4. EDX of pure $ZnCo_2O_4$ (**a**) and $ZnCo_2O_4/SnO_2$-20% (**b**) nanoparticles.

Infrared characterization, FTIR, was carried out to verify the existence of the spinel structure in the prepared photocatalysts. The spinel structure oxides have two distinct bands in the wavenumber range between 400 and 700 cm^{-1}. FTIR spectra presented in Figure 5 for all samples, show the presence of two strong peaks at 660 and 570 cm^{-1} resulting from M–O stretching modes for the tetrahedral coordination of Zn and M–O vibrational mode for the octahedrally coordinated Co ions, respectively, which confirms the formation of the spinel structure [36–38]. The introduction of SnO_2 seems to disturb the spinel matrix as the band at 570 cm^{-1} is modified with the SnO_2 increase. A peak appears in the region in the range of 440–560 cm^{-1} which can indicate the presence of SnO_2 and can correspond to O–Sn–O and Sn–O stretching vibration modes [39]. For wavenumbers higher than 1000, the four signals were flat.

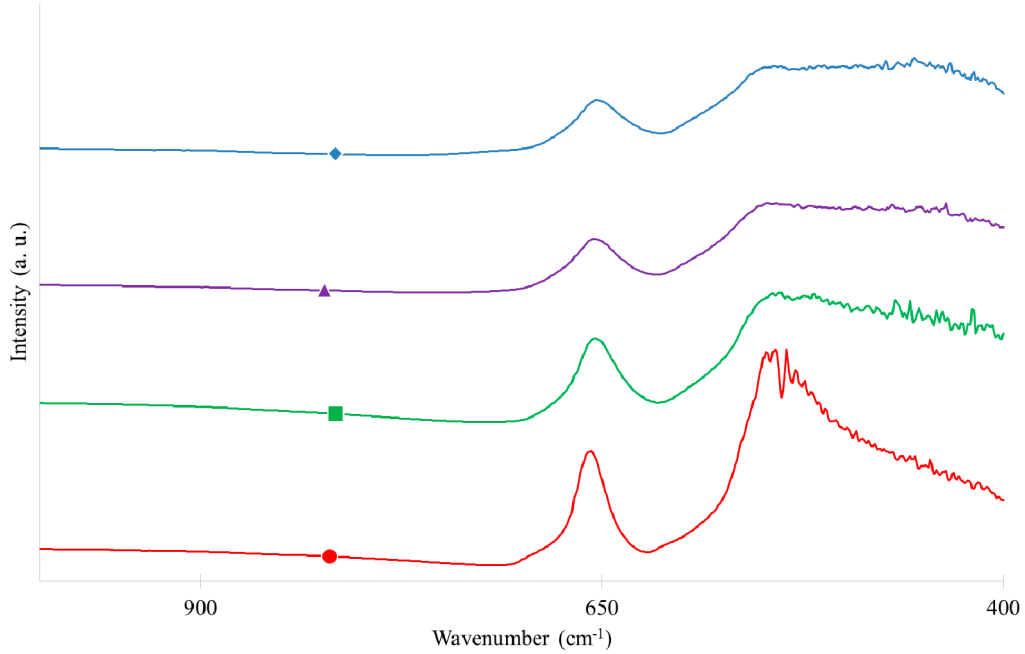

Figure 5. Fourier-transformed infrared spectroscopy (FTIR) spectra of (●) pure $ZnCo_2O_4$, (■) $ZnCo_2O_4/SnO_2$-10%, (▲) $ZnCo_2O_4/SnO_2$-20% and (♦) $ZnCo_2O_4/SnO_2$-30%.

Figure 6 shows the XPS spectra for pure $ZnCo_2O_4$ and $ZnCo_2O_4/SnO_2$-20% which was representative of all samples modified by SnO_2. Figure 6a represent the spectra of the Zn 2p with Zn 2p3/2 and Zn 2p1/2 located around 1021.1 eV and 1044.1 eV for pure $ZnCo_2O_4$ and 1021.3 eV and 1044.3 eV for $ZnCo_2O_4/SnO_2$-20%. The sharp peaks correspond to the bivalent zinc ions [16,40]. The oxidation state of the Zn in $ZnCo_2O_4$ is further confirmed by the Auger parameter which is equal to 2011.2 eV [41]. Unfortunately, the Auger parameter in the $ZnCo_2O_4/SnO_2$-20% cannot be calculated due to interference of the Sn3d peak with the Zn Auger line.

Concerning Co, (Figure 6b), three peaks were found around 779.7 eV, 789.4, 794.6 eV, and 805.0 eV and were similar for all samples. The peaks at 779.7 eV and 794.6 eV correspond to the Co 2p3/2 and Co 2p1/2 [16] and can be attributed to Co^{3+} ions in octahedral sites [16,42]. This signal is similar to the standard signal of Co_3O_4 [43], but also to that of $ZnCo_2O_4$, as both compounds are hard to distinguish by XPS technique. The satellite peaks located at around 789.5 eV and 805 eV further confirm that cobalt's oxidation number is +3 and not +2 [44].

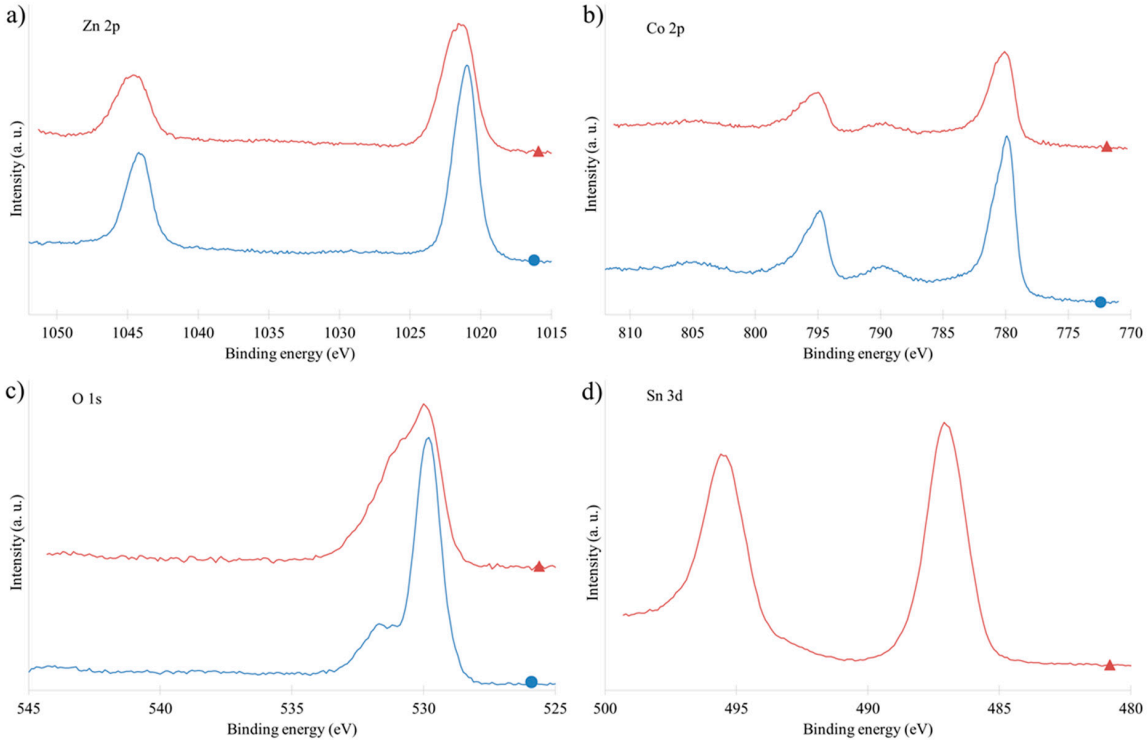

Figure 6. X-ray photoelectron spectroscopy (XPS) spectra of (●) pure $ZnCo_2O_4$ and (▲) $ZnCo_2O_4/SnO_2$-20%: (**a**) Zn 2p region, (**b**) Co 2p region, (**c**) O 1s region and (**d**) Sn 3d region.

The O 1s signal was represented on Figure 6c and was typical for the metal-oxygen framework [45,46]. The modification of the overall shape of the O 1s signal (Figure 6c) is due to a different binding energy for the oxygen atom in the SnO_2 structure compared to the $ZnCo_2O_4$ structure. The former binding energy is 530.6 eV [47], slightly higher than the latter, as Figure 6c shows.

Concerning the Sn signal (Figure 6d), two peaks were observed around 486.9 eV and 495.4 eV in all modified samples corresponding to Sn^{4+} [48] which is characteristic of SnO_2. This is confirmed by the Auger parameter value of 919.2 eV which is correspond to SnO_2.

Thus, we know that all elements are in their expected oxidation state and chemical environment.

2.2. *Optical Properties*

The modification of the $ZnCo_2O_4$ structure and the variation of its optical properties due to the incorporation of tin dioxide were followed by UV–Vis absorption spectroscopy whose objective is the determination of band gap energies. The normalized absorption spectra obtained are shown in Figure 7. As described in [13,16], the absorption range of all $ZnCo_2O_4$ materials are in the range of 250–800 nm. Absorption in visible is well observed and so, a photoactivity with this type of illumination is expected (see Section 3.3). Due to the large absorption, it is not possible to determine a band gap value with the classical method (i.e., Kubelka-Monk functions). For comparison, the spectrum of Evonik P25 is measured (Figure 7). For this material, no absorption in visible range is observed. The photoactivity is thus expected to be lower than the $ZnCo_2O_4$ materials (see Section 3.3). The direct and indirect band gap values for P25 are 3.42 and 2.99 eV, respectively, as previously reported [28,49].

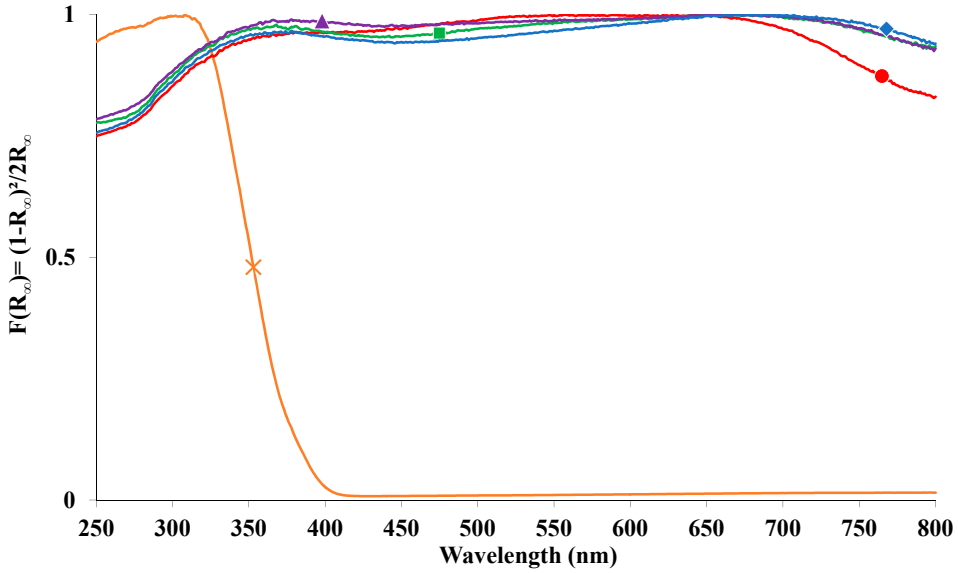

Figure 7. UV–Visible absorption spectra of (●) pure $ZnCo_2O_4$, (■) $ZnCo_2O_4/SnO_2$-10%, (▲) $ZnCo_2O_4/SnO_2$-20%, (♦) $ZnCo_2O_4/SnO_2$-30% and (×) Evonik P25.

2.3. Photocatalytic Performance

The study of the photocatalytic activity was studied by comparing the photocatalytic activities of the four materials by using PNP solutions at 14 mg/L and confirmed by CR solutions with two different concentrations (20 mg/L and 35 mg/L). The partial order of the reaction relative to the pollutant was determined by comparing both CR degradation experiments. Let us consider the rate *r* [mol/L/h] as

$$r = -\frac{dC}{dt} = kC^{\alpha} \Rightarrow kt = \frac{C_0^{\alpha}}{(1-\alpha)}\left(1-\left(\frac{C}{C_0}\right)^{1-\alpha}\right) \quad (1)$$

where C is the concentration of CR [mol/L], t is the time [h], k is the rate constant (whose unit depends on α), α is the partial order of the reaction relative to CR, and C_0 is the initial concentration of CR. The coefficient of variation was calculated for each set of experiments, where the initial concentration was varied using the same photocatalyst. The average coefficient of variation (across all experiments) was minimized using a GRG nonlinear method and was equal to 0.003. We will consider that the reaction is a zero-order one, since the value of 0.003 is very close to 0. While pseudo-first orders are often reported for photocatalysis, zero orders are not unseen for congo red and could denote a very strong adsorption of CR by the various photocatalysts [50,51]. The values of the constants for PNP and CR are represented in Table 2.

Table 2. Zero-order rate constants for the degradation of p-nitrophenol and congo red.

Sample	k_{PNP} (10^{-7} mol/L/h)	$\bar{k}_{CR}$ (10^{-7} mol/L/h)
No catalyst	0	0
P25	5	2.1
Pure $ZnCo_2O_4$	13.3	5.9
$ZnCo_2O_4/SnO_2$-10%	17.9	7.1
$ZnCo_2O_4/SnO_2$-20%	27.9	12.0
$ZnCo_2O_4/SnO_2$-30%	19.2	9.8

It is difficult to compare our photocatalysts adequately with other reports from the literature, because many parameters are varied, like the nature of the catalyst, the nature of the degraded molecule, concentrations, volumes, intensity and frequency of the spectrum of light, or temperature, amongst

the most obvious ones. Typical values are in the range of what we found for CR, with e.g., Shaban et al. [52] finding a 21.5×10^{-7} mol/L/h rate with MCM48/Ni_2O_3 concentrated at 0.2 g/L.

The results obtained on CR after 6 h of irradiation with visible radiation (λ > 400 nm) at pH = 8 and at room temperature (Figure 8) clearly show that the incorporation of tin dioxide (SnO_2) positively improved the photocatalytic activity of zinc cobaltite ($ZnCo_2O_4$). Indeed, the degradation percentages increased from 57% with pure $ZnCo_2O_4$ to 91% with $ZnCo_2O_4$/SnO_2-20% samples for a dye concentration of 20 mg/L and from 24% to 63% for a dye concentration of 35 mg/L. The SnO_2 addition increases the activity in both cases. When the amount of SnO_2 increases to 30 wt %, although the photocatalytic activity remains higher than the pure sample (82–47% versus 57–24% with 20 mg/L and 30 mg/L of dye solution, respectively), the photocatalytic activity decreases compared to $ZnCo_2O_4$/SnO_2-20% sample. This observation indicates that an optimal loading content is reached for $ZnCo_2O_4$/SnO_2-20% sample.

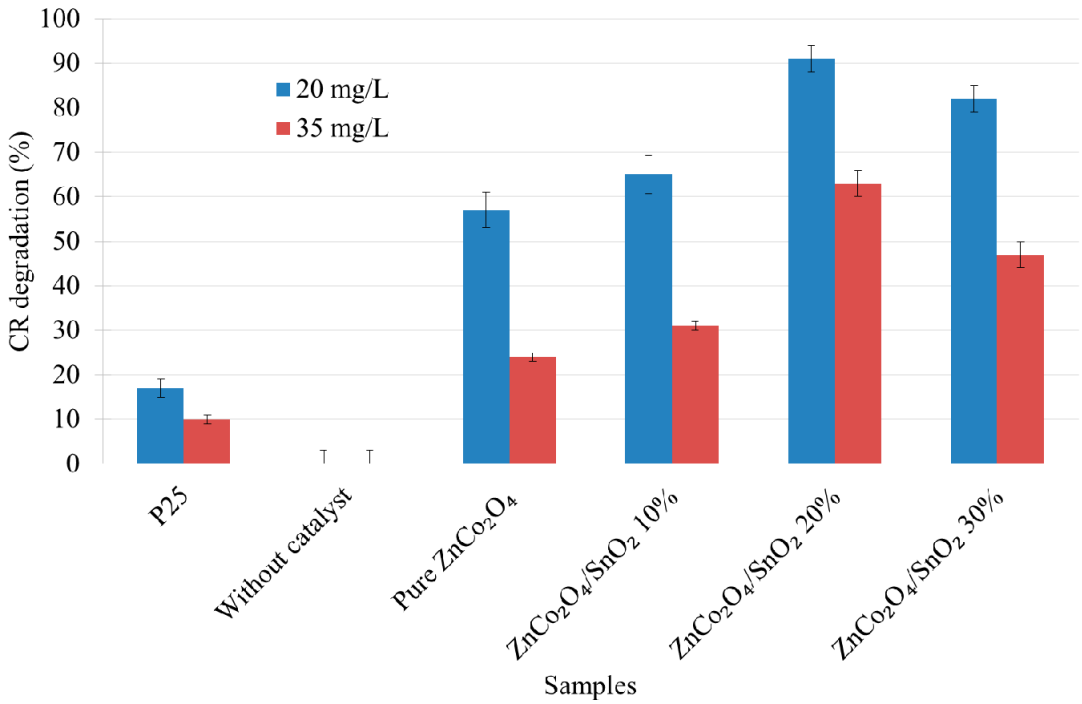

Figure 8. CR degradation (%) without catalyst and for all the samples under visible light (λ > 400 nm) after 6 h of illumination.

For the PNP degradation, similar observations can be made after 24 h of illumination (Figure 9), the PNP degradation increased when the photocatalyst is modified with SnO_2. An optimal degradation rate is also observed when the amount of SnO_2 is 20%. A comparison with commercial Evonik P25 shows that the $ZnCo_2O_4$ based catalysts are more active under visible light with a PNP degradation rate three to six times higher than P25 for all samples (Figure 9). The PNP degradations can be compared to previous modified-TiO_2 materials under similar photocatalytic conditions [53,54]: In these works, visible activated TiO_2 doped with Fe and N reached 42 and 69% of PNP degradation respectively with the best materials after 24 h of visible illumination. In this work, the highest PNP degradation was obtained with $ZnCo_2O_4$/SnO_2-20% reaching 67% after 24 h of illumination. As mentioned above, it is difficult to compare our materials with other works as a lot of photocatalytic conditions were different (lamp intensity, illumination time, concentration, etc.).

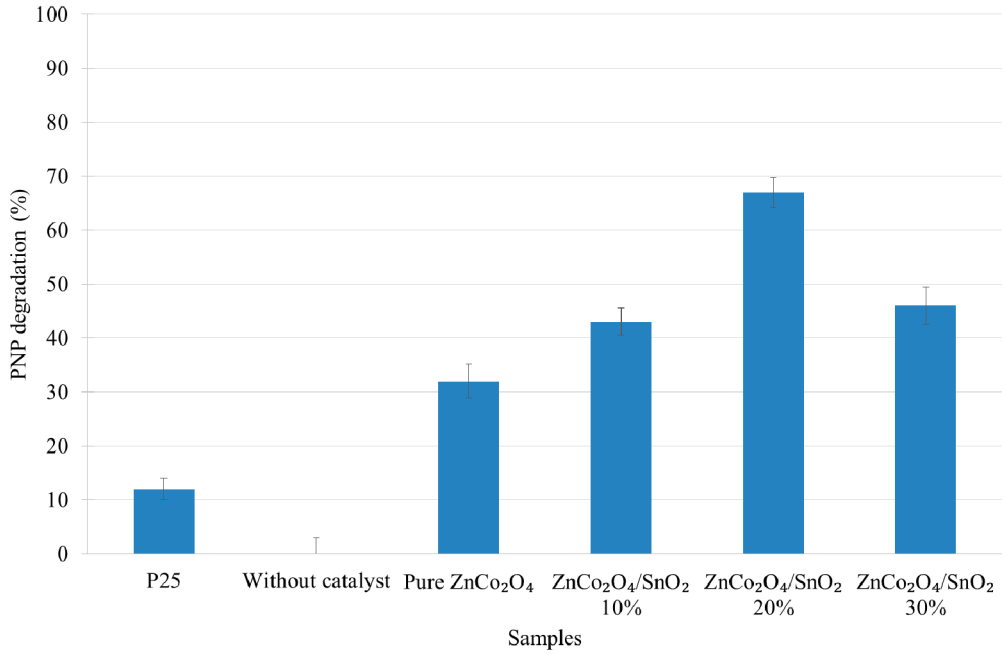

Figure 9. *p*-Nitrophenol (PNP) degradation (%) without catalyst and for all the samples under visible light after 24 h of illumination.

Concerning the improvement of the photocatalytic activity with the modification with SnO_2 addition, two effects can be detailed: A modification of the textural and morphological property and the formation of heterojunction between $ZnCo_2O_4$ and SnO_2.

Concerning the formation of heterojunction, this mixed oxide can increase the photoactivity by increasing the recombination time between the charges (electrons (e^-) and holes (h^+)). The mechanism is described in Figure 10. Indeed, it is possible to calculate the conduction and valence band potentials [55–57] of $ZnCo_2O_4$ and SnO_2 with their estimated band gap (2.26 [58] and 3.63 [59] eV, respectively). The calculated energy levels for both oxides are represented in Figure 10. The mechanism in the mixed oxide is interpreted as follows: When the samples are illuminated with visible light, the $ZnCo_2O_4$ materials are excited producing photogenerated e^- and h^+. Part of the photogenerated electrons can be displaced on the SnO_2 conduction band (CB). The photogenerated electron–hole pairs will be separated effectively in the $ZnCo_2O_4/SnO_2$ mix oxide [60]. So, the recombination of photogenerated species can be restrained. The efficient charge separation could increase the lifetime of the charge carriers and gives enough time to react with the reactants adsorbed onto the photocatalyst surfaces to improve the photocatalytic activity.

Moreover, as the CB of $ZnCo_2O_4$ (−0.69 eV) is more negative than that of potential of $O_2/{\cdot}O_2^-$ (−0.285 V versus NHE) [60], the adsorbed O_2 was easily reduced to ${\cdot}O_2^-$ by the $ZnCo_2O_4$. But the valence band (VB) potential of $ZnCo_2O_4$ (1.57 eV) was insufficient to generate ·OH radicals (${\cdot}OH/H_2O$ potential, 2.30 eV versus NHE) [60]. Nevertheless, ·OH can be produced from the ${\cdot}O_2^-$ by reacting with a proton in water [16].

On the other hand, the textural properties of $ZnCo_2O_4/SnO_2$-20% sample could also explain its higher photocatalytic activity. Indeed, the specific surface area is the highest for this sample. Compared to the Evonik P25 catalyst, $ZnCo_2O_4/SnO_2$-20% sample presents a five to six times increase regarding the degradation percentage (i.e., 17 an 10% of CR degradation regarding Evonik P25 catalyst for 20 mg/L and 30 mg/L of dye solution respectively and 12% of PNP degradation).

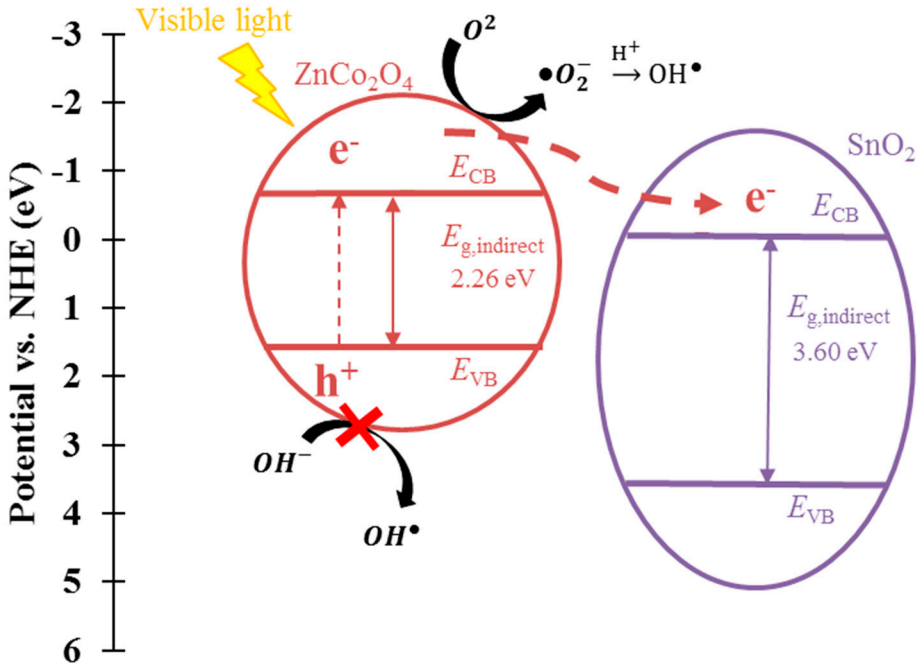

Figure 10. Mechanism of charge transfer in mixed SnO_2-$ZnCo_2O_4$ sample. Electrons (e^-) and holes (h^+) correspond to the photogenerated electron and hole, E_{CB} and E_{CV} stand for potentials of conduction and valence band, $E_{g,indirect}$ corresponds to the indirect band gap.

For example, with CR, the photocatalytic activity can be divided by the specific surface area to highlight the importance of this parameter (Figure 11a). It is observed that the activity is the highest for the pure sample but the difference between samples decreases when the pollutant concentration increases. Indeed, when the amount of pollutant increases, a lot of active sites are mandatory for reaction and so, an increased specific surface area would favor the degradation activity. If the specific surface area is low, even an efficient catalyst will have its activity limited by its number of active sites. So, the specific surface area becomes a very crucial parameter to obtain an efficient photoactivity with a high concentration of pollutant.

Moreover, the SnO_2 addition in the loaded samples seems to present a low crystallinity (Figure 1) as the diffraction peaks are very weak. As this SnO_2 fraction probably has a low photocatalytic activity, it can be suggested that the effect of SnO2 is not entirely linked to a photochemical phenomenon but rather to a textural effect. In this optic, the photoactivity per surface area can be linked to the real mass of $ZnCo_2O_4$ present in the samples tanks to Equation (2) (Figure 11b).

$$CR\ degradation\ per\ m^{-2}\ and\ g^{-1}_{ZnCo_2O_4} = \frac{CR\ degradation\ (\%)}{S_{BET} * M_{ZnCo_2O_4}} \quad (2)$$

where $M_{ZnCo_2O_4}$ corresponds to the mass of $ZnCo_2O_4$ in the sample and can be calculated with Equation (3).

$$M_{ZnCo_2O_4} = M_{photocatalyst} - M_{SnO_2} \quad (3)$$

where $M_{photocatalyst}$ corresponds to the total mass of photocatalyst used for the catalytic experiment and M_{SnO_2} corresponds to the mass of SnO_2 in the sample.

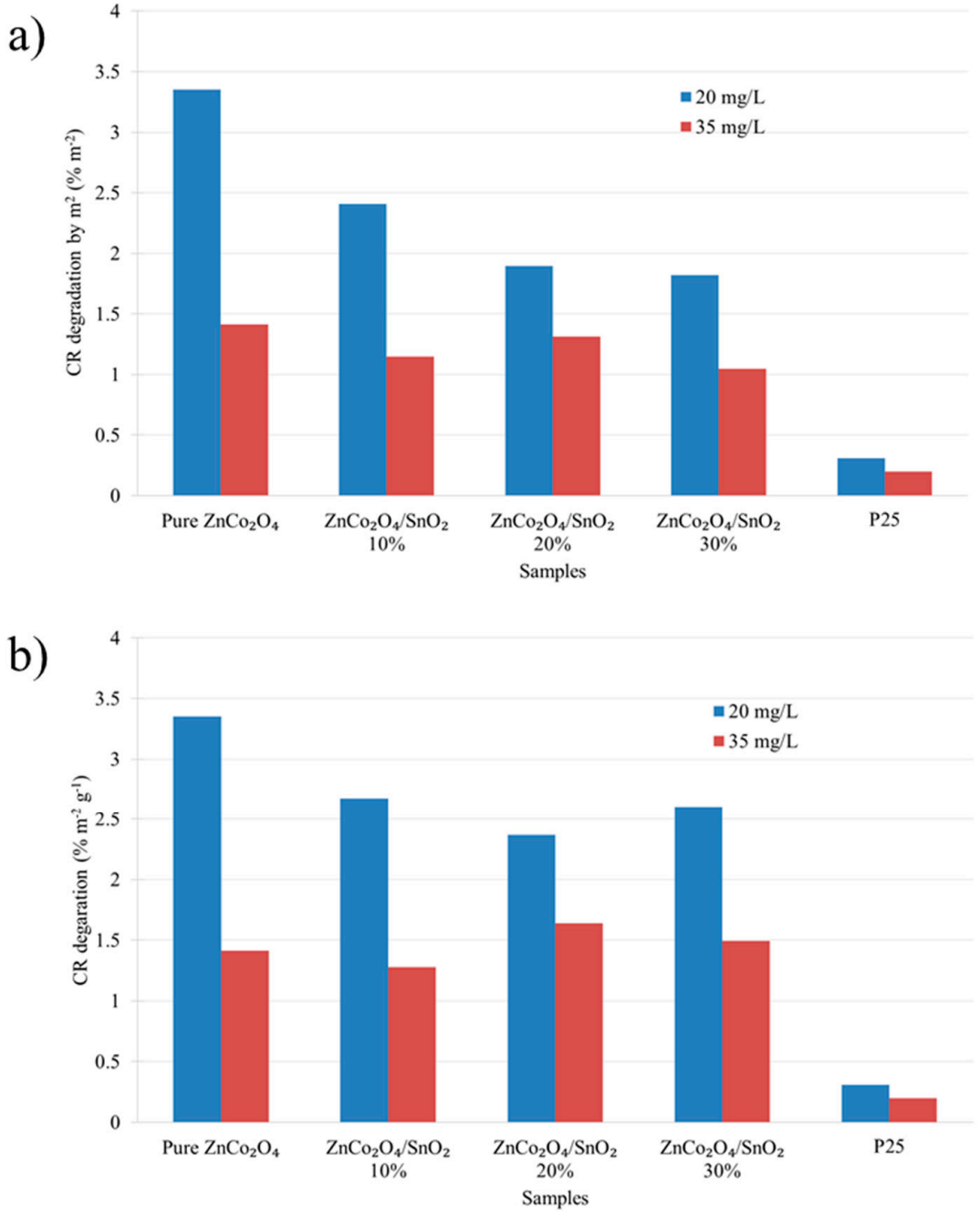

Figure 11. (**a**) CR degradation per m^2 (% m^{-2}) for all the samples under visible light (λ > 400 nm) after 6 h of illumination; and (**b**) CR degradation per m^2 and per g of $ZnCo_2O_4$ (% $m^{-2}{\cdot}g^{-1}$) for all the samples under visible light (λ > 400 nm) after 6 h of illumination. For the Evonik P25, the photoactivity is reported to the mass of TiO_2.

In this case, the CR degradation (with an initial concentration of 35 mg/L) is higher when the sample is loaded with 20% of SnO_2 compared to the other samples. From these results, it can be deduced that the SnO_2 loading increases the photoactivity of degradation by a modification of the specific surface area and therefore by an increase in the contact surface area between the catalyst and the pollutant. In other words, the photoefficiency of $ZnCo_2O_4$ per unit mass increases when the specific surface increases. The SnO_2 increase to 30 wt % of SnO_2 leads to a small decrease of specific surface area and consequently a loss of activity compared to the 20 wt % sample, this observation can reinforce the fact that the activity is linked to the morphology of the sample.

A comparison with literature shows that CR degradation is widely studied [25–27] but the conditions of testing are quite different from a work to another making the comparison difficult. In Srivind et al. [25], the complete degradation of CR appears after about 3 h of illumination by light containing UV parts. However, the catalyst and dye concentrations are different from our study and the catalyst used is a nearly pure SnO_2. In Ehsan et al. [26], the used catalysts are ZnO materials. The degradation of CR is obtained after 40 min with a very low initial concentration (75 ppm) and an UV–visible illumination. In Akika et al. [27], CR is degraded is about 3 h with Cu-$NiAl_2O_4$ catalyst under solar light containing UV-part. Once again, the CR and catalyst concentrations are very different from our test. Through literature, it is difficult to find exactly the same catalytic tests with similar conditions, especially for the lamp.

2.4. Photocatalytic Stability

The photocatalytic activity stability of the samples were assessed on five consecutive photocatalytic experiments on PNP degradation, for a total duration of 120 h. The mean PNP degradation is represented on Figure 12 for all samples. For all photocatalysts, the activity in maintains on 120 h of illumination, keeping at 90% of their initial activity. These experiments show the great stability of the $ZnCo_2O_4$ samples staying far more efficient than Evonik P25 on the PNP degradation.

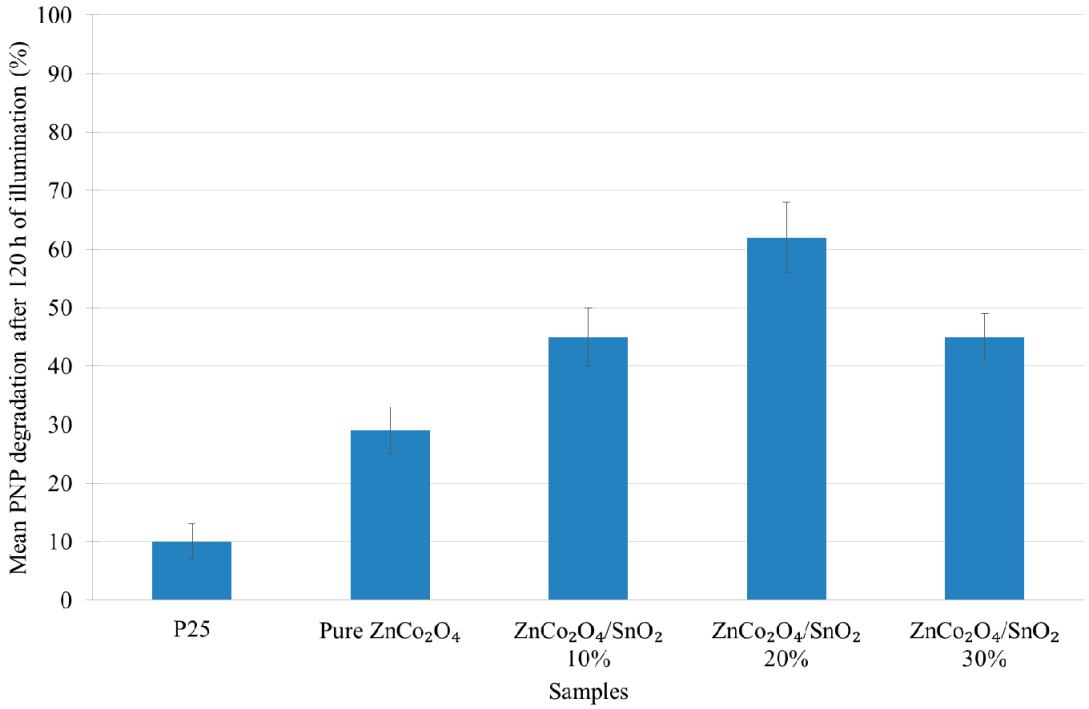

Figure 12. Mean PNP degradation (%) under visible light for all samples after the four recycling cycles (corresponding to five catalytic tests of 24 h each, with isolation of the sample and drying stages in between).

Moreover, the morphology and the crystallinity after the four recycling cycles for pure $ZnCo_2O_4$ and $ZnCo_2O_4/SnO_2$-20% were also assessed (Figure 13). No modification was observed when comparing the final SEM pictures and XRD diffractograms with initial morphology (Figure 3) and crystallinity (Figure 1).

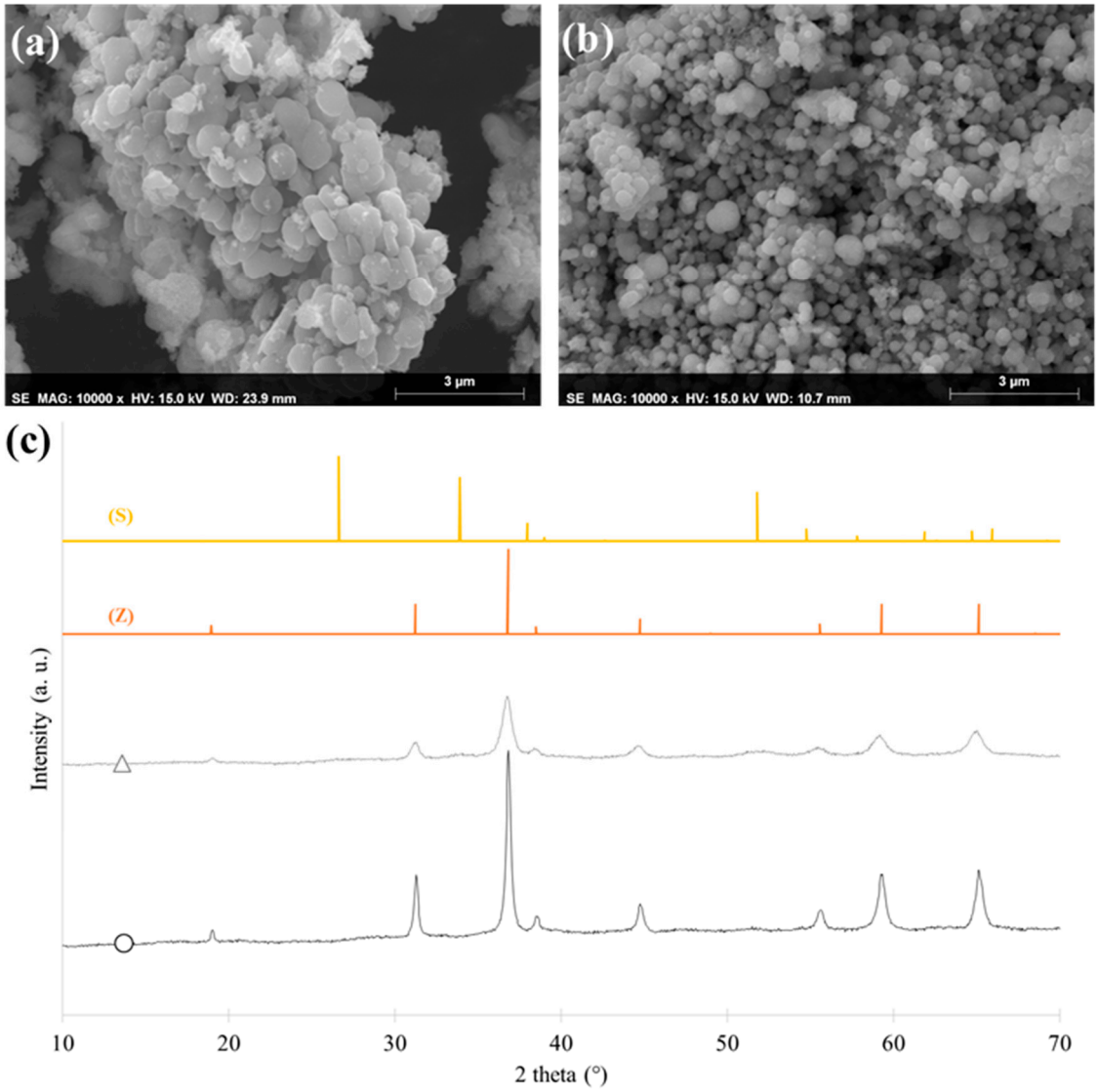

Figure 13. SEM images of pure $ZnCo_2O_4$ (**a**) and $ZnCo_2O_4/SnO_2$-20% (**b**) samples after the four recycling cycles. (**c**) XRD patterns of (○) pure $ZnCo_2O_4$ and (Δ) $ZnCo_2O_4/SnO_2$-20% after the four recycling cycles. (Z) Reference pattern of cubic spinel ZnCo2O4 and (S) reference pattern of tetragonal rutile SnO_2.

3. Materials and Methods

3.1. Chemicals

All the reagents used in our experiments were of analytical purity and were used as received: Zinc acetate dehydrates (BIOCHEM, Cosne Cours sur Loire, France), oxalic acid dihydrate (Chemopharma, Cosne Cours sur Loire, France), lithium nitrate, sodium nitrate, potassium nitrate, and ethanol (Sigma-Aldrich, St. Louis, MO, USA).

3.2. Material Synthesis

In order to develop the materials by sol-gel process [37,61], two solutions were prepared separately. Solution 1 ($ZnCo_2O_4$) was obtained by dissolving cobalt nitrate hexahydrate and zinc nitrate tetrahydrate in ethanol. The compounds were sources of cobalt and zinc, respectively, and produced Solution 1. Solution 2 (SnO_2) was prepared from tin chloride dihydrate as precursor and ethanol as solvent. The two solutions were mixed to obtain the $SnO_2/ZnCo_2O_4$ sample which, after

evaporation, turned into a gel. Drying the gel at 110 °C and then calcining it at 450 °C led to a crystallized powder. The detailed synthesis protocol is presented on the flowchart of the Figure 14.

Four materials were produced: Pure $ZnCo_2O_4$, $ZnCo_2O_4/SnO_2$-10%, $ZnCo_2O_4/SnO_2$-20%, and $ZnCo_2O_4/SnO_2$-30%.

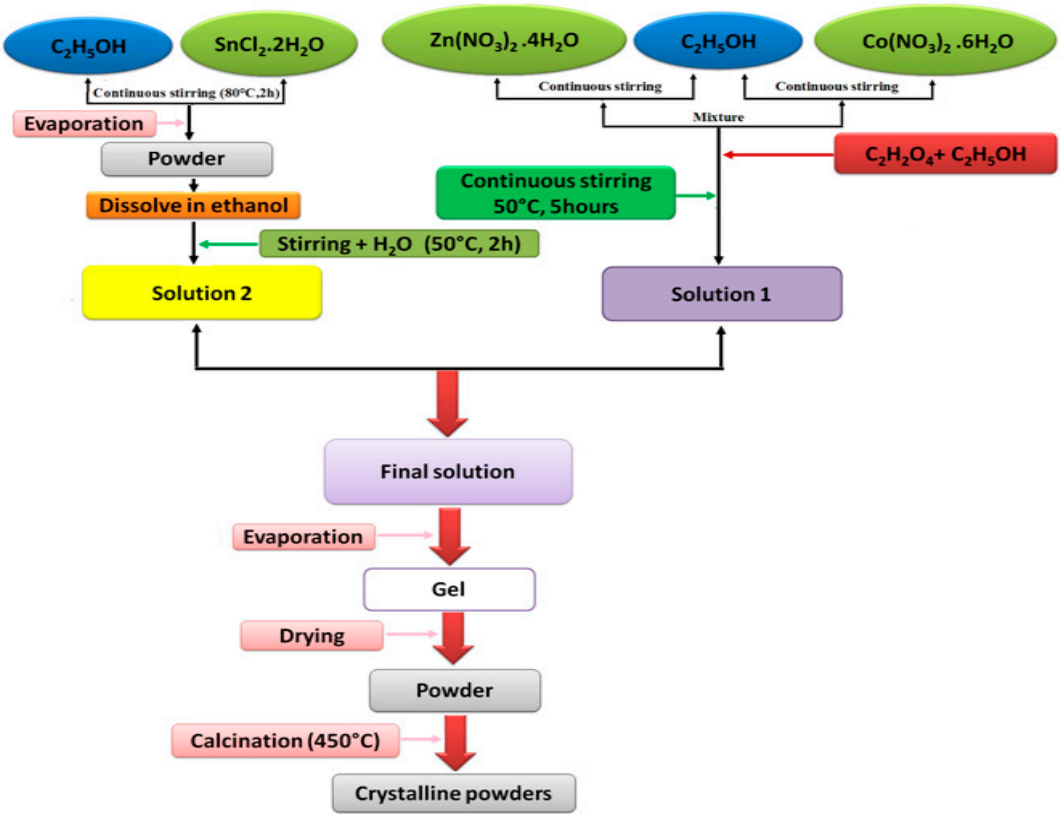

Figure 14. Process for sol-gel synthesis of $ZnCo_2O_4$ and SnO_2 loaded $ZnCo_2O_4$.

3.3. Material Characterization

The actual amount of SnO_2 in the SnO_2-loaded $ZnCo_2O_4$ sample was determined by inductively coupled plasma–atomic emission spectroscopy (ICP–AES), equipped with an ICAP 6500 THERMO Scientific device (Thermo Fisher Scientific, Waltham, MA, USA). Solutions for analysis were prepared as follows [62]: (i) 2 g of Na_2O_2, 1 g of NaOH and 0.1 g of sample were mixed in a vitreous carbon crucible; (ii) the mixture was heated beyond the melting point (up to 950 °C); (iii) after cooling and solidification, the mixture was digested in 30 mL of HNO_3 (65%); (iv) the solution was then transferred into a 500 mL calibrated flask that was finally filled with deionized water. The solution was then analyzed using an ICP-AES device.

X-ray powder diffraction analysis was realized using a Bruker D8 Twin-Twin powder diffractometer using Cu Kα radiation (Bruker, Billerica, MA, USA). The XRD pattern was identified by comparison with the JCPD standard. The crystalline size, d_{XRD}, was determined by using the Scherrer equation based on line broadening analysis [63],

$$d_{XRD} = \frac{0,9\,\lambda}{\beta\,\cos\,\theta} \quad (4)$$

where, λ is the corrected wavelength of the X-radiation, β the full width at half-maximum corrected for instrumental broadening, and θ is the Bragg angle of the diffraction peak.

SEM micrographs were obtained using a Jeol-JSM-6360LV microscope (JEOL, Peabody, MA, USA) under high vacuum at an acceleration voltage of 20 kV. An elemental analysis by EDX was also performed.

FTIR spectra were carried out using an IRAffinity-1S device from Shimadzu in ATR mode (Shimadzu, Kyoto, Japan). The following instrumental settings were used: Absorbance, range from 4000 to 400 cm^{-1}, 30 scans, and resolution 2 cm^{-1}.

The sample textural properties were characterized by nitrogen adsorption-desorption isotherms in an ASAP 2420 multi-sampler adsorption-desorption volumetric device from Micromeritics (Micromeritics, Norcross, GA, USA). From these isotherms, the microporous volume was calculated using Dubinin-Radushkevich theory (V_{DR}). The surface area was evaluated using Brunauer, Emmett, and Teller theory (S_{BET}) [35].

The sample optical properties were evaluated by using diffuse reflectance spectroscopy measurements in the 250–850 nm region with a Lambda 1050 S UV/VIS/NIR spectrophotometer form PerkinElmer, equipped with an integrating sphere (150mm InGaAs Int. Sphere from PerkinElmer Waltham, MA, USA) and using Al_2O_3 as reference. The absorbance spectra were transformed using the Kubelka–Munk function [10,64,65] to produce a signal, normalized for comparison between samples, and so to calculated the band gaps (Eg,direct and Eg,indirect). The details of this treatment method have been widely described elsewhere [53,54,66].

The chemical states of the elements present in the samples were determined by XPS analysis with an Escalab 250Xi device from Thermo Scientific (Waltham, MA, USA). Spectra were acquired with monochromatic Al Kα source (1486.6 eV) and using a spot size of 500 µm and pass energy of 20 eV (for high resolution spectra). The photoelectrons were collected at an angle of 0° relative to the sample surface normal. A flood gun using combined electron and low energy ions was also used during analysis to prevent surface charging. The binding energies were corrected in order to have the C1s binding energy at 285.0 eV.

3.4. Photocatalytic Activity under Visible Light

The degradation of PNP was studied under visible light (λ > 400 nm) to determine the photocatalytic activity of the synthesized material. The potential of the material was confirmed through the degradation of congo dye (CR). The lamp was a halogen lamp covered by a UV filter (cutoff wavelength = 420 nm, intensity at 395 nm reduced by 95%), the lamp had a continuous spectrum from 400 to 800 nm (300 W, 220 V), as measured with a Mini-Spectrometer TM-UV/vis C10082MD from Hamamatsu (Hamamatsu, Japan).

Photocatalytic experiments were conducted in test tubes closed with a sealing cap. These tubes were placed in a cylindrical glass reactor [67] with the halogen lamp in the center. The reactor was maintained at constant temperature (20 °C) by a cooling system with recirculating water. The lamp was also cooled by a similar system. Aluminum foil covered the outer wall of the reactor to prevent any interaction with the room lighting. For each tested catalyst, three flasks with catalyst were exposed to light to assess the CR and PNP degradation. A blank measurement had been performed to ensure that Congo red did not degrade under illumination alone. For each catalyst, a dark test had also been performed to ensure that the samples did not adsorb the dye significantly. The evolution of the CR and PNP concentrations was measured by UV–Vis spectroscopy (GENESYS 10S UV–Vis from Thermo Scientific, Waltham, MA, USA) between 300 and 800 nm, using a calibration curve performed with different concentrations of CR and PNP to ensure the linearity of the absorbance and pollutant concentration.

The initial concentrations of the Congo red dye were 20 mg/L and 35 mg/L. In each tube, the catalyst concentration was 0.5 g/L. For the PNP, the initial concentration was 14 mg/L with a catalyst concentration of 1 g/L. The commercial Evonik P25 was used as reference material.

3.5. Recycling Study

To test the stability of the photoactivity of samples, photocatalytic recycling tests are made on all samples under visible light for the PNP degradation. The same protocol as explained in the above paragraph (Section 3.4) is performed on all catalysts. After this, the samples are recovered by centrifugation (10,000 rpm for 1 h) followed by drying at 120 °C for 24 h. A total of four photocatalytic tests as described above are applied to the re-used catalysts. So, each tested catalyst undergoes five catalytic tests (120 h of operation), and a mean PNP degradation over the recycling tests is then calculated.

The morphology and the crystallinity after the four recycling cycles are characterized with SEM and XRD on two samples: Pure $ZnCo_2O_4$ and $ZnCo_2O_4/SnO_2$-20%.

4. Conclusions

In this work, pure and SnO_2 loaded $ZnCo_2O_4$ photocatalysts have been synthesized by the sol-gel process. Three different SnO_2 loading ratios were obtained: 10, 20, and 30 wt %. Their photocatalytic activities were assessed on the degradation of two organic pollutants in water under visible illumination.

The physico-chemical characterizations have shown that the materials are composed of crystalline $ZnCo_2O_4$ matrix with a crystallite size that decreases with the amount of SnO_2. For the loaded samples, weakly crystalline SnO_2 is observed. The specific surface area is modified with the loading ratio. Indeed, it increases with the loading content with an optimal value for the sample loaded with 20 wt % of SnO_2. The FTIR spectra confirms the existence of the spinel structure in the samples of the prepared photocatalysts. The diffuse reflectance measurements show that all samples had a strong absorption in the 250 and 800 nm range. The XPS measurements show that all elements are in their expected oxidation state and chemical environment.

The evaluation of the photoactivity of the samples under visible light for the degradation of *p*-nitrophenol shows that all materials are highly photoactive under visible light. They are also able to degrade congo red efficiently. The SnO_2 loading increases the activity compared to the pure sample. The main factor of this improvement can be due to the formation of a $SnO_2/ZnCo_2O_4$ mixed oxide with an increased charge separation.

A second factor could be the addition of SnO_2 which also increases of the specific surface area. Indeed, the best sample with 20 wt % of SnO_2 has a specific surface area three times higher than the pure samples. The photoactivity has been reported to material surface area and the mass of $ZnCo_2O_4$ present in all samples. It appears that, especially at high concentration, the increase of the specific surface area becomes a crucial parameter to improve photoefficiency.

The photocatalyst activity stability has been also assessed under five consecutive photocatalytic experiments (120 h of illumination) showing a constant activity over time. Moreover, the morphology and the crystallinity stayed constant after 120 h of use.

A comparison with commercial Evonik P25 shows that the materials developed in this work have a five to six fold increase in efficiency under visible light, leading to a promising photocatalyst material.

Author Contributions: Conceptualization, H.B., S.K. and J.G.M.; methodology, H.B., S.K., C.W. and J.G.M.; material synthesis, H.B., B.A. and R.B.; material characterization, J.G.M., R.G.T., H.B., S.K., B.A., V.C., A.F., P.L. and R.B.; resources, S.D.L.; writing—original draft preparation, J.G.M. and H.B.; writing—review and editing, J.G.M., R.G.T., C.W., V.C., A.F. and S.D.L.; supervision, S.D.L. and J.G.M.; funding acquisition, S.D.L. and J.G.M.

Funding: This research received no external funding.

Acknowledgments: S.D.L. thanks the Belgian National Funds for Scientific Research (F.R.S.-FNRS) for her Senior Associate Researcher position. R.T. benefits from funding of the Fund for Scientific Research (F.R.S.-FNRS) under a Fund for Research Training in Industry and Agriculture (FRIA) grant. The authors are grateful to Dirk Poelman, from Ghent University, for diffuse reflectance spectroscopy measurements. The authors also thank the Ministère de la Région Wallonne Direction Générale des Technologies, de la Recherche et de l'Energie (DG06) and the Fonds de Recherche Fondamentale Collective.

Conflicts of Interest: The authors declare no conflict of interest.

References

1. Vosoughifar, M. Preparation, characterization, and morphological control of $MnWO_4$ nanoparticles through novel method and its photocatalyst application. *J. Mater. Sci. Mater. Electron.* **2017**, *28*, 2135–2140. [CrossRef]
2. Shah, M.P. Industrial Wastewater Treatment: A Challenging Task in the Industrial. *Adv. Recycl. Waste Manag.* **2016**, *2*, 115. [CrossRef]
3. Bhatkhande, D.S.; Pangarkar, V.G.; Beenackers, A.A.C.M. Photocatalytic degradation for environmental applications—A review. *J. Chem. Technol. Biotechnol.* **2001**, *77*, 102–106. [CrossRef]
4. Azam, A.; Ahmed, A.S.; Oves, M. Size-dependent antimicrobial properties of CuO nanoparticles against Gram-positive and -negative bacterial strains. *Int. J. Nanomed.* **2012**, *7*, 3527–3535. [CrossRef] [PubMed]
5. Léonard, G.L.-M.; Pàez, C.A.; Ramírez, A.E.; Mahy, J.G.; Heinrichs, B. Interactions between Zn^{2+} or ZnO with TiO_2 to produce an efficient photocatalytic, superhydrophilic and aesthetic glass. *J. Photochem. Photobiol. A Chem.* **2018**, *350*, 32–43. [CrossRef]
6. Tian, Q.; Wei, W.; Dai, J.; Sun, Q.; Zhuang, J.; Zheng, Y.; Liu, P.; Fan, M.; Chen, L. Porous core-shell $Ti_xSn_{1-x}O_2$ solid solutions with broad-light response: One-pot synthesis and ultrahigh photooxidation performance. *Appl. Catal. B Environ.* **2019**, *244*, 45–55. [CrossRef]
7. Wu, M.; Leung, D.Y.C.; Zhang, Y.; Huang, H.; Xie, R.; Szeto, W.; Li, F. Toluene degradation over Mn-TiO_2/CeO_2 composite catalyst under vacuum ultraviolet (VUV) irradiation. *Chem. Eng. Sci.* **2019**, *195*, 985–994. [CrossRef]
8. Pelaez, M.; Nolan, N.T.; Pillai, S.C.; Seery, M.K.; Falaras, P.; Kontos, A.G.; Dunlop, P.S.M.; Hamilton, J.W.J.; Byrne, J.A.; O'Shea, K.; et al. A review on the visible light active titanium dioxide photocatalysts for environmental applications. *Appl. Catal. B Environ.* **2012**, *125*, 331–349. [CrossRef]
9. Linsebigler, A.L.; Lu, G.; Yates, J.T. Photocatalysis on TiO_2 Surfaces: Principles, Mechanisms, and Selected Results. *Chem. Rev.* **1995**, *95*, 735–758. [CrossRef]
10. Malengreaux, C.M.; Douven, S.; Poelman, D.; Heinrichs, B.; Bartlett, J.R. An ambient temperature aqueous sol-gel processing of efficient nanocrystalline doped TiO_2-based photocatalysts for the degradation of organic pollutants. *J. Sol-Gel Sci. Technol.* **2014**, *71*, 557–570. [CrossRef]
11. Lee, A.; Libera, J.A.; Waldman, R.Z.; Ahmed, A.; Avila, J.R.; Elam, J.W.; Darling, S.B. Conformal Nitrogen-Doped TiO_2 Photocatalytic Coatings for Sunlight-Activated Membranes. *Adv. Sustain. Syst.* **2017**, *1*, 1600041. [CrossRef]
12. Li, J.; Wang, J.; Wexler, D.; Shi, D.; Liang, J.; Liu, H.; Xiong, S.; Qian, Y. Simple synthesis of yolk-shelled $ZnCo_2O_4$ microspheres towards enhancing the electrochemical performance of lithium-ion batteries in conjunction with a sodium carboxymethyl cellulose binder. *J. Mater. Chem. A* **2013**, *1*, 15292–15299. [CrossRef]
13. Chen, J.; Zhan, J.; Lu, E.; Wan, Y.; Jin, Z.; Qi, H. Facile template-free fabrication of mesoporous $ZnCo_2O_4$ fibers with enhanced photocatalytic activity under visible-light irradiation. *Mater. Lett.* **2018**, *220*, 66–69. [CrossRef]
14. Liu, B.; Liu, H.; Liang, M.; Liu, L.; Lv, Z.; Zhou, H.; Guo, H. Controlled synthesis of hollow octahedral $ZnCo_2O_4$ nanocages assembled by untrathin 2D nanosheets for enhanced lithium storage. *Nanoscale* **2017**, *9*, 17174–17180. [CrossRef] [PubMed]
15. Kim, T.W.; Woo, M.A.; Regis, M.; Choi, K. Electrochemical Synthesis of Spinel Type $ZnCo_2O_4$ Electrodes for Use as Oxygen Evolution Reaction Catalysts. *J. Phys. Chem. Lett.* **2014**, *5*, 2370–2374. [CrossRef] [PubMed]
16. Goswami, K.; Ananthakrishnan, R.; Mandal, S. Facile synthesis of cation doped ZnO-$ZnCo_2O_4$ hetero-nanocomposites for photocatalytic decomposition of aqueous organics under visible light. *Mater. Chem. Phys.* **2018**, *206*, 174–185. [CrossRef]
17. Sarkar, A.; Karmakar, K.; Khan, G.G. Designing Co-Pi Modified One-Dimensional *n–p* TiO_2/$ZnCo_2O_4$ Nanoheterostructure Photoanode with Reduced Electron—Hole Pair Recombination and Excellent Photoconversion Efficiency (>3%). *J. Phys. Chem. C* **2017**, *121*, 25705–25717. [CrossRef]
18. Rashid, J.; Barakat, M.A.; Mohamed, R.M.; Ibrahim, I.A. Enhancement of photocatalytic activity of zinc/cobalt spinel oxides by doping with ZrO_2 for visible light photocatalytic degradation of 2-chlorophenol in wastewater. *J. Photochem. Photobiol. A Chem.* **2014**, *284*, 1–7. [CrossRef]

19. Valverde Aguilar, G.; Jaime Fonseca, M.R.; Mantilla Ramirez, A.; Juarez Gracia, A.G. Photoluminescence Studies on ZnO Thin Films Obtained by Sol-Gel Method. In *Recent Applications in Sol-Gel Synthesis*; Intechopen: London, UK, 2017; pp. 197–212.
20. Bodson, C.J.; Heinrichs, B.; Tasseroul, L.; Bied, C.; Mahy, J.G.; Wong Chi Man, M.; Lambert, S.D. Efficient P- and Ag-doped titania for the photocatalytic degradation of waste water organic pollutants. *J. Alloys Compd.* **2016**, *682*, 144–153. [CrossRef]
21. Bischoff, B.; Anderson, M. Peptization Process in the Sol-Gel Preparation of Porous Anatase (TiO_2). *Chem. Mater.* **1995**, *7*, 1772–1778. [CrossRef]
22. Gratzel, M. Sol-gel processed TiO_2 films for photovoltaic applications. *J. Sol-Gel Sci. Technol.* **2001**, *22*, 7–13. [CrossRef]
23. Mahy, J.G.; Deschamps, F.; Collard, V.; Jérôme, C.; Bartlett, J.; Lambert, S.D.; Heinrichs, B. Acid acting as redispersing agent to form stable colloids from photoactive crystalline aqueous sol–gel TiO_2 powder. *J. Sol-Gel Sci. Technol.* **2018**, *87*, 568–583. [CrossRef]
24. Belet, A.; Wolfs, C.; Mahy, J.G.; Poelman, D.; Vreuls, C. Sol-gel Syntheses of Photocatalysts for the Removal of Pharmaceutical Products in Water. *Nanomaterials* **2019**, *9*, 126. [CrossRef] [PubMed]
25. Balamurugan, J.S.S.; Prabha, K.U.D.; Nagarethinam, M.S.V.S. Visible light irradiated photocatalytic and magnetic properties of Fe-doped SnS_2 nanopowders. *J. Mater. Sci. Mater. Electron.* **2018**, *29*, 9016–9024.
26. Ehsan, M.F.; Bashir, S.; Hamid, S.; Zia, A.; Abbas, Y.; Umbreen, K.; Naeem, M.; Shah, A. One-pot facile synthesis of the ZnO/ZnSe heterostructures for e ffi cient photocatalytic degradation of azo dye. *Appl. Surf. Sci.* **2018**, *459*, 194–200. [CrossRef]
27. Akika, F.Z.; Benamira, M.; Lahmar, H.; Tibera, A.; Chabi, R.; Avramova, I.; Suzer, Ş.; Trari, M. Structural and optical properties of Cu-substitution of $NiAl_2O_4$ and their photocatalytic activity towards Congo red under solar light irradiation. *J. Photochem. Photobiol. A Chem.* **2018**, *364*, 542–550. [CrossRef]
28. Mahy, J.G.; Paez, C.A.; Carcel, C.; Bied, C.; Tatton, A.S.; Damblon, C.; Heinrichs, B.; Wong Chi Man, M.; Lambert, S.D. Porphyrin-based hybrid silica-titania as a visible-light photocatalyst. *J. Photochem. Photobiol. A Chem.* **2019**, *373*, 66–76. [CrossRef]
29. Rochkind, M.; Pasternak, S.; Paz, Y. Using dyes for evaluating photocatalytic properties: A critical review. *Molecules* **2015**, *20*, 88–110. [CrossRef]
30. Zhu, Y.; Cao, C.; Zhang, J.; Xu, X. Two-dimensional ultrathin $ZnCo_2O_4$ nanosheets: General formation and lithium storage application. *J. Mater. Chem. A* **2015**, *3*, 9556–9564. [CrossRef]
31. Qiu, Y.; Yang, S.; Deng, H.; Li, W. A novel nanostructured spinel $ZnCo_2O_4$ electrode material: Morphology conserved transformation from a hexagonal shaped nanodisk precursor and application in lithium ion batteries. *J. Mater. Chem.* **2010**, *20*, 4439–4444. [CrossRef]
32. Léonard, G.L.-M.; Malengreaux, C.M.; Mélotte, Q.; Lambert, S.D.; Bruneel, E.; Van Driessche, I.; Heinrichs, B. Doped sol–gel films vs. powders TiO_2: On the positive effect induced by the presence of a substrate. *J. Environ. Chem. Eng.* **2016**, *4*, 449–459. [CrossRef]
33. Bhagwat, A.D.; Sawant, S.S.; Ankamwar, B.G.; Mahajan, C.M. Synthesis of Nanostructured Tin Oxide (SnO_2) Powders and Thin Films Prepared by Sol-Gel Method. *J. Nano- Electron. Phys.* **2015**, *7*, 04037.
34. Singh, R.P.P.; Hudiara, I.S.; Panday, S.; Rana, S.B. Effect of Ni Doping on Structural, Optical, and Magnetic Properties of Fe-Doped ZnO Nanoparticles. *J. Supercond. Nov. Magn.* **2015**, *28*, 3685–3691. [CrossRef]
35. Lecloux, A. Exploitation des isothermes d'adsorption et de désorption d'azote pour l'étude de la texture des solides poreux. *Mémoires Société des Sciences de Liege Belgium* **1971**, *1*, 169–209.
36. Kustova, G.N.; Burgina, E.B.; Volkova, G.G.; Yurieva, T.M.; Plyasova, L.M. IR spectroscopic investigation of cation distribution in Zn–Co oxide catalysts with spinel type structure. *J. Mol. Catal. A Chem.* **2000**, *158*, 293–296. [CrossRef]
37. Wei, X.; Chen, D.; Tang, W. Preparation and characterization of the spinel oxide $ZnCo_2O_4$ obtained by sol-gel method. *Mater. Chem. Phys.* **2007**, *103*, 54–58. [CrossRef]
38. Barakat, N.A.M.; Khil, M.S.; Sheikh, F.A.; Kim, H.Y. Synthesis and Optical Properties of Two Cobalt Oxides (CoO and Co_3O_4) Nanofibers Produced by Electrospinning Process. *J. Phys. Chem. C* **2008**, *112*, 12225–12233. [CrossRef]
39. Paramarta, V.; Taufik, A.; Saleh, R. Better adsorption capacity of SnO_2 nanoparticles with different graphene addition. *J. Phys. Conf. Ser.* **2016**, *776*, 012039. [CrossRef]

40. Druska, P.; Steinike, U.; Šepelák, V. Surface structure of mechanically activated and of mechanosynthesized zinc ferrite. *J. Solid State Chem.* **1999**, *146*, 13–21. [CrossRef]
41. Biesinger, M.C.; Lau, L.W.M.; Grosvenor, A.P.; Smart, R.S.C. Resolving surface chemical states in XPS analysis of first row transition metals, oxides and hydroxides: Sc, Ti, V, Cu and Zn. *Appl. Surf. Sci.* **2010**, *257*, 887–898. [CrossRef]
42. Chuang, T.J.; Brundle, C.R.; Rice, D.W. Interpretation of the x-ray photoemission spectra of cobalt oxides and cobalt oxide surfaces. *Surf. Sci.* **1976**, *59*, 413–429. [CrossRef]
43. Biesinger, M.C.; Payne, B.P.; Grosvenor, A.P.; Lau, L.W.M.; Gerson, A.R.; Smart, R.S.C. Resolving surface chemical states in XPS analysis of first row transition metals, oxides and hydroxides: Cr, Mn, Fe, Co and Ni. *Appl. Surf. Sci.* **2011**, *257*, 2717–2730. [CrossRef]
44. Oku, M.; Hirokawa, K. X-ray photoelectron spectroscopy of Co_3O_4, Fe_3O_4, Mn_3O_4, and related compounds. *J. Electron Spectros. Relat. Phenom.* **1976**, *8*, 475–481. [CrossRef]
45. Yuan, C.; Li, J.; Hou, L.; Lin, J.; Zhang, X.; Xiong, S. Polymer-assisted synthesis of a 3D hierarchical porous network-like spinel $NiCo_2O_4$ framework towards high-performance electrochemical capacitors. *J. Mater. Chem. A* **2013**, *1*, 11145–11151. [CrossRef]
46. Lu, Y.; Lin, Y.; Wang, D.; Wang, L.; Xie, T.; Jiang, T. A high performance cobalt-doped ZnO visible light photocatalyst and its photogenerated charge transfer properties. *Nano Res.* **2011**, *4*, 1144–1152. [CrossRef]
47. Moses, P.R.; Wier, L.M.; Lennox, J.C.; Finklea, H.O.; Lenhard, J.R.; Murray, R.W. X-ray photoelectron spectroscopy of alkylaminesilanes bound to metal oxide electrodes. *Anal. Chem.* **1978**, *50*, 576–585. [CrossRef]
48. Ben Haj Othmen, W.; Hamdi, A.; Addad, A.; Sieber, B.; Elhouichet, H.; Szunerits, S.; Boukherroub, R. Fe-doped SnO_2 decorated reduced graphene oxide nanocomposite with enhanced visible light photocatalytic activity. *J. Photochem. Photobiol. A Chem.* **2018**, *367*, 145–155. [CrossRef]
49. Janus, M.; Morawski, A.W. New method of improving photocatalytic activity of commercial Degussa P25 for azo dyes decomposition. *Appl. Catal. B Environ.* **2007**, *75*, 118–123. [CrossRef]
50. Hachem, C.; Bocquillon, F.; Zahraa, O.; Bouchy, M. Decolourization of textile industry wastewater by the photocatalytic degradation process. *Dyes Pigments* **2001**, *49*, 117–125. [CrossRef]
51. Devi, L.G.; Kumar, S.G.; Reddy, K.M. Photo fenton like process $Fe^{3+}/(NH_4)_2\ S_2O_8$/UV for the degradation of Di azo dye congo red using low iron concentration. *Cent. Eur. J. Chem.* **2009**, *7*, 468–477.
52. Shaban, M.; Abukhadra, M.R.; Hamd, A.; Amin, R.R.; Abdel Khalek, A. Photocatalytic removal of Congo red dye using MCM-48/Ni_2O_3 composite synthesized based on silica gel extracted from rice husk ash; fabrication and application. *J. Environ. Manag.* **2017**, *204*, 189–199. [CrossRef] [PubMed]
53. Mahy, J.G.; Lambert, S.D.; Léonard, G.L.-M.; Zubiaur, A.; Olu, P.-Y.; Mahmoud, A.; Boschini, F.; Heinrichs, B. Towards a large scale aqueous sol-gel synthesis of doped TiO_2: Study of various metallic dopings for the photocatalytic degradation of p-nitrophenol. *J. Photochem. Photobiol. A Chem.* **2016**, *329*, 189–202. [CrossRef]
54. Mahy, J.G.; Cerfontaine, V.; Poelman, D.; Devred, F.; Gaigneaux, E.M.; Heinrichs, B.; Lambert, S.D. Highly efficient low-temperature N-doped TiO_2 catalysts for visible light photocatalytic applications. *Materials* **2018**, *11*, 584. [CrossRef] [PubMed]
55. Tian, J.; Shao, Q.; Zhao, J.; Pan, D.; Dong, M.; Jia, C.; Ding, T. Microwave solvothermal carboxymethyl chitosan templated synthesis of TiO_2/ZrO_2 composites toward enhanced photocatalytic degradation of Rhodamine B. *J. Colloid Interface Sci.* **2019**, *541*, 18–29. [CrossRef] [PubMed]
56. Renuka, L.; Anantharaju, K.S.; Vidya, Y.S.; Nagaswarupa, H.P.; Prashantha, S.C. A simple combustion method for the synthesis of multi-functional ZrO_2/CuO nanocomposites: Excellent performance as Sunlight photocatalysts and enhanced latent fingerprint detection. *Appl. Catal. B Environ.* **2017**, *210*, 97–115. [CrossRef]
57. Xu, Y.; Schoonen, M.A.A. The absolute energy positions of conduction and valence bands of selected semiconducting minerals. *Am. Mineral.* **2000**, *85*, 543–556. [CrossRef]
58. Amini, M.N.; Dixit, H.; Saniz, R.; Lamoen, D.; Partoens, B. The origin of p-type conductivity in ZnM_2O_4 (M = Co, Rh, Ir) spinels. *Phys. Chem. Chem. Phys.* **2014**, *16*, 2588–2596. [CrossRef]
59. Benhebal, H.; Chaib, M.; Léonard, A.; Lambert, S.D.; Crine, M. Synthesis, characterization and photocatalytic properties of alkali metals doped tin dioxide. *J. Mol. Struct.* **2011**, *1004*, 222–226. [CrossRef]

60. Yi, S.; Yue, X.; Xu, D.; Liu, Z.; Zhao, F.; Wang, D.; Lin, Y. Study on photogenerated charge transfer properties and enhanced visible-light photocatalytic activity of p-type Bi_2O_3/n-type ZnO heterojunctions. *New J. Chem.* **2015**, *39*, 2917–2924. [CrossRef]
61. Novinrooz, A.; Sarabadani, P.; Garouse, J. Characterization of Pure and Antimony Doped SnO_2 Thin Films Prepared by the Sol-Gel Technique. *Iran. J. Chem. Chem. Eng.* **2006**, *25*, 31–38.
62. Mahy, J.G.; Tasseroul, L.; Zubiaur, A.; Geens, J.; Brisbois, M.; Herlitschke, M.; Hermann, R.; Heinrichs, B.; Lambert, S.D. Highly dispersed iron xerogel catalysts for p-nitrophenol degradation by photo-Fenton effects. *Microporous Mesoporous Mater.* **2014**, *197*, 164–173. [CrossRef]
63. Reenu, J.; Harikrishnan, N.; Jayakumari, I. Structural and Morphological Studies of Nano-crystalline Ceramic $BaSr_{0.9}Fe_{0.1}TiO_4$. *Int. Lett. Chem. Phys. Astron.* **2015**, *41*, 100–117.
64. Kubelka, P.; Munk, F. Ein Beitrag zur Optik der Farban striche. *Z. Tech. Phys.* **1931**, *12*, 593–603.
65. Kubelka, P. New contributions to the optics of intensely light-scattering materials. *J. Opt. Soc. Am.* **1948**, *38*, 448–457. [CrossRef] [PubMed]
66. Malengreaux, C.M.; Pirard, S.L.; Léonard, G.; Mahy, J.G.; Herlitschke, M.; Klobes, B.; Hermann, R.; Heinrichs, B.; Bartlett, J.R. Study of the photocatalytic activity of Fe^{3+}, Cr^{3+}, La^{3+} and Eu^{3+} single-doped and co-doped TiO_2 catalysts produced by aqueous sol-gel processing. *J. Alloys Compd.* **2017**, *691*, 726–738. [CrossRef]
67. Páez, C.A.; Liquet, D.Y.; Calberg, C.; Lambert, S.D.; Willems, I.; Germeau, A.; Pirard, J.P.; Heinrichs, B. Study of photocatalytic decomposition of hydrogen peroxide over ramsdellite-MnO_2 by O_2-pressure monitoring. *Catal. Commun.* **2011**, *15*, 132–136. [CrossRef]